



Modelling heat transfer for a tubular micro-solid oxide fuel cell with experimental validation

Saeid Amiri^{a,1}, R.E. Hayes^{a,*}, K. Nandakumar^{a,2}, Partha Sarkar^b

^a Department of Chemical and Materials Engineering, University of Alberta, Edmonton, AB, Canada T6G 2G6

^b Alberta Innovates – Technology Futures, Edmonton, AB, Canada T6N 1E4

HIGHLIGHTS

- Non-isothermal model for a micro SOFC.
- Experimental validation.
- The heat transfer is shown not to have a strong effect.

ARTICLE INFO

Article history:

Received 9 October 2012

Received in revised form

9 January 2013

Accepted 11 January 2013

Available online 23 January 2013

Keywords:

Solid oxide fuel cell

Heat transfer

Modelling

Local heat generation

ABSTRACT

A detailed mathematical model that accounts for mass, momentum, heat, and electric charge transfer is developed for a tubular micro-solid oxide fuel cell. Electrochemical reactions as well as reversible and irreversible heat generation are modelled locally within the volume of each cermet electrode. The gas velocity profile and convective and conductive heat and mass transfer are modelled within each porous electrode and the gas channel. The heat transfer model includes the thermal radiation exchanged between surfaces.

The simulation results are validated against electrochemical performance and temperature distribution experimental data. Simulation results are presented to give a detailed insight about several aspects of the cell's thermal behaviour. It is found that local heating within the electrodes is negligible when the temperature is controlled on the surface of the electrode. Temperature gradients along the cell's active length are found not to be negligible. Modelling heat transfer has a negligible effect on overall cell performance predictions for the specific setup of this study.

© 2013 Elsevier B.V. All rights reserved.

1. Introduction

The performance of a solid oxide fuel cell (SOFC) is strongly temperature dependent because the electric conductivity of the electrolyte and the electrodes' electrochemical activity are highly temperature dependent. In fact, SOFC operates at high temperature primarily because conventional SOFC electrolytes function, i.e. conduct ions, at high temperatures. In addition to electric power, a SOFC generates heat while operating, and experiments have shown that the temperature difference between the cell surface and inlet gas can be up to hundreds of degrees Celsius [1]. While

SOFC systems consisting of only a few cells need externally supplied heating to maintain them at their operating temperature, larger stacks are not only thermally self-sufficient, but removing the generated heat is a major challenge. If heat is not removed effectively, hot-spots can form, which are detrimental to the cell performance and durability. Hot-spots increase agglomeration, degradation, and thermal stresses within the cell components. On the other hand, cells below optimal temperature can significantly reduce the stack performance. Therefore, maintaining a uniform temperature within a SOFC stack is critical for both the reliability and optimal performance of the system.

Experimentally studying the thermal behaviour of a SOFC is challenging, and mathematical modelling and simulation can provide detailed information about the thermal and electrochemical performances. A validated mathematical model of a SOFC can also provide significant insight into thermal effects not accessible through experimentation. In addition, modelling the electrochemical performance of SOFC is not possible without considering

* Corresponding author. Tel.: +1 780 492 3571; fax: +1 780 492 2881.

E-mail address: bob.hayes@ualberta.ca (R.E. Hayes).

¹ Present address: Wave Control Systems, Edmonton, AB, Canada T6E 0C1.

² Present address: Cain Department of Chemical Engineering, Louisiana State University, Baton Rouge, LA 70803, USA.

its thermal behaviour, because reaction rates and material properties are highly temperature dependent. Many mathematical models for the SOFC are presented in the literature for a wide range of geometries, designs, and operating conditions. Few of these studies include heat transfer effects, and even fewer incorporate a complete treatment of it. For example some papers include heat transfer but ignore thermal radiation [1–23], use simplified radiation models [24], use heat transfer coefficients for thermal convection [25,26], use empirical transfer coefficients for heat or mass transport modelling [26,27], ignore gas flow [20,28,29], do not include detailed models for electrodes [10,15,17–19,27,28,30–33], assume heat generation only at the electrode/electrolyte interface [13,14,16,34–36], or use overall reaction heat generation instead of single electrode [1,6,7,9,35,37,38]. Some excellent reviews summarize the ongoing efforts on the thermal modelling of SOFC [39–42].

The focus of this paper is a tubular micro-SOFC (T_{μ} SOFC) developed at the Alberta Research Council in Canada. A detailed model is developed for a single cell to simulate the phenomena occurring within its tens-of-micron-thick electrodes and electrolyte layers, as well as its centimetre-wide gas channels. These phenomena include heat and mass transfer, fluid flow, electric current flow, and electrochemical reactions. The reactions are assumed to occur within the volume of the composite electrode, enabling the model to account for the extent of the reaction zone. The reversible heating was included, and was based on single-electrode entropy generation, calculated locally at each point within each electrode. Irreversible heat generation was also estimated within the volume of SOFC layers. Physical properties of materials were calculated based on local conditions, i.e. temperature, pressure, and composition. Experimental data obtained especially for validation purposes are presented and compared with simulation results. Based on kinetic parameters estimated in our previous work for 800 °C isothermal conditions, and without any further performance curve fitting, the purely predictive simulation results were found to be consistent with non-isothermal experimental results for a range of temperatures.

The aim of this work is to develop a detailed model for a single T_{μ} SOFC and to validate it experimentally. The emphasis of this work, and a unique aspect of it, is the comprehensive electrochemical performance and heat transfer validation of such detailed model based on experiments conducted specifically on the particular T_{μ} SOFC. Of the few studies that include heat transfer in their models, even fewer include experimental validation. Of those, some include validation but lack radiation completely [2,3,43–48], use simplified radiation models [49–51], omit the detail modelling of electrodes [2,3,52,53], use lumped heat generation models instead of detailed estimation of single electrode heat generation [49,54,55], assume reactions occur only at the interface of electrolyte/electrode [46,47,56], use benchmark data or experimental data from other literature [3,25,45–47,50,51,53,56], validate the electrochemical performance but not the thermal model [5,43,49,51,55,57]. A model on heat transfer should ideally be validated for heat transfer, as a fuel cell model should be for electrochemical performance. This work presents specific experimental data for both aspects, performance curves at various temperature, as well as temperature distribution within the system and aims at experimental validation of the model both in terms of thermal and electrochemical performances. A validated single-cell model is a stepping stone for reliably developing a stack model and making predictions thereafter.

The validated model was used to investigate the thermal behaviour of the T_{μ} SOFC. A detailed temperature distribution profile was obtained. The effect of non-isothermal conditions on cell performance was assessed. Insights useful for the experimenter

are discussed, such as the temperature rise within the cell layers due to heat generation, the temperature gradients along the cell, the effect of non-isothermal conditions on cell performance, and the magnitude of temperature rise when under constant furnace load. Validated for a single cell, the model can be further extended to model a stack of fuel cells, which can be a significant developmental and diagnostic tool.

2. Experimental

The T_{μ} SOFC was an anode supported cell with composite cermet electrodes as shown in Fig. 1. A detailed description of the fabrication process can be found elsewhere [58,59]. The 7 cm long cell was 2.5 mm in diameter, with a 2.5 cm active length. This active length had 6 layers, see Fig. 1. These layers are: anode current collector (ACCL), anode support (ASL), anode functional (AFL), electrolyte, cathode functional (CFL), and cathode current collector (CCCL). Current collector layers were porous gold, the electrolyte was dense, YSZ, ASL and AFL were porous Ni/YSZ composites, and CFL was a porous LSM/YSZ composite. The inactive length of the cell was not covered by CFL and CCCL, however it had all the remaining layers; the dense electrolyte layer prevented any mixing of hydrogen flowing inside the cell with air. The cell had one end open and the other closed. An alumina fuel injector tube was used inside. The anode current collector layer was extended from the active length inside the cell to the open end, covering a small length on the outer surface of the cell, where the anode wire was wrapped around it.

Fig. 2 shows a multi-scale schematic of the test setup. The fuel cell was at the centre of a single-zone tubular electric furnace such

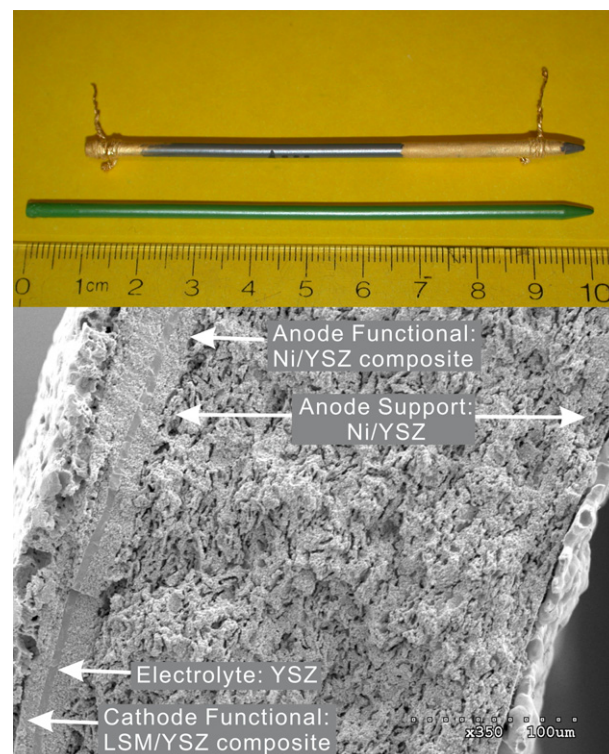


Fig. 1. The anode supported T_{μ} SOFC. Top: an incomplete cell fabricated by electrophoretic deposition (EPD), before adding the cathode functional layer, the current collectors, and the wiring (green) and a complete cell after reduction (grey). Bottom: a SEM micrograph of the anode supported T_{μ} SOFC cross section (For interpretation of the references to colour in this figure legend, the reader is referred to the web version of this article.).

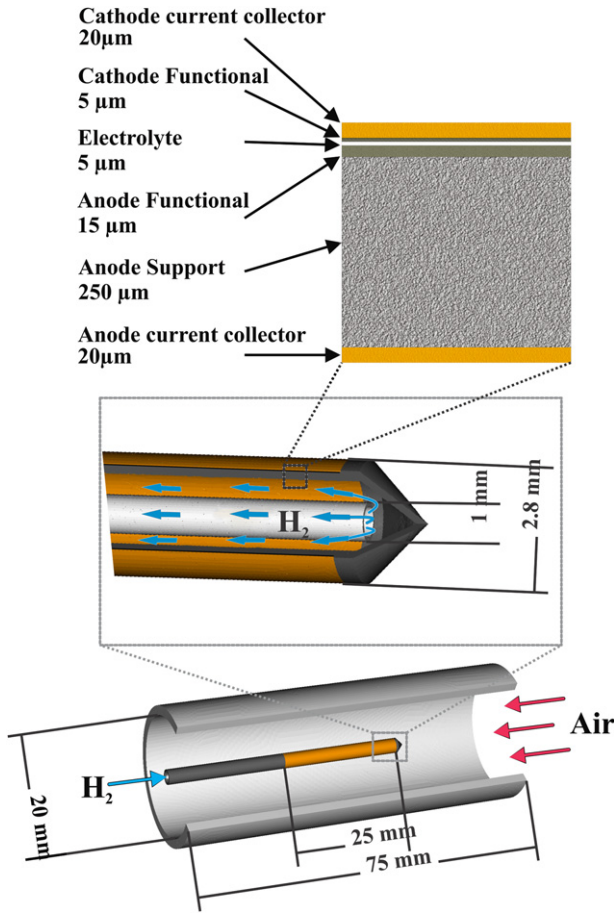


Fig. 2. A multi-scale schematic of the anode TμSOFC: the cell within the furnace (bottom); the tip of the cell, indicating the injector tube (middle); the layers of the active length (top).

that cell's active length and the furnace tube were aligned along a common axis. Five thin thermocouples measured the temperature distribution within the furnace, as shown in Fig. 3. Three thermocouples, sheathed in 1.5 mm OD alumina rods, were

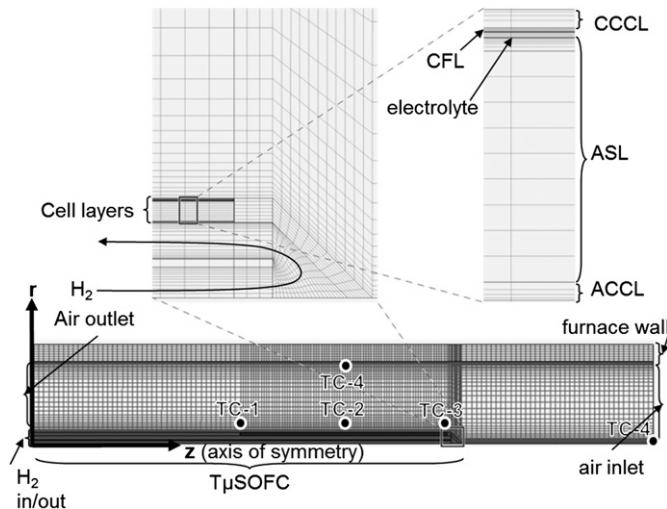


Fig. 3. The structured mesh used to discretize the computational domain and thermocouples locations in the furnace.

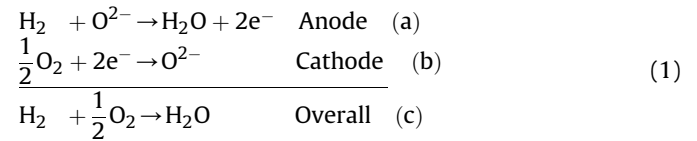
attached along the cell to measure the temperature of the active length at the middle and two ends (TC-1, TC-2, TC-3); two thermocouple wires measured the temperature of the inlet air flow (TC-5), and that of the furnace inner wall at the middle (TC-4). A PID controller was used to keep TC-2 at the desired temperature. Performance of the cell was measured by an Agilent N3301A electronic load, equipped with an Agilent N3302A cartridge. An in-house computer program was used to collect and control cell performance data and temperature readings. Details of experimental procedures can be found in Ref. [59].

3. Model development

3.1. Physical description

On the SOFC cathode side, oxygen is transported through the bulk gas and porous layers to the cathode's active sites, where it is converted to oxide ions by consuming electrons. The oxide ions are then conducted through the dense, but ion permeable electrolyte, to the anode side. On the anode side, hydrogen is transported through the anode's gas channel and the porous layers to the anode's active sites, where it reacts with the oxygen ions to produce electrons and water vapour. Water is transported back through the porous electrode to the anode's gas channel, whence it is carried out with the gas flow.

The electrochemical reactions in a hydrogen SOFC with an oxygen permeable electrolyte are given in equation (1). Electrochemical reactions occur at three phase boundaries (TPB) where the electronic conductor, the ionic conductor and the gas phase intersect. In composite porous electrodes TPB are extended from the electrode/electrolyte interface to the electrode's volume, which enhances the electrode performance by providing more reaction sites.



The chemical non-equilibrium between the anode and cathode drives the electrochemical reaction, and creates an electric potential difference between electrodes. By allowing the electrons to flow from the anode to the cathode, the change in the Gibbs free energy change of cell's overall reaction is harvested. In reality, however, the voltage of a cell drops as current is drawn from it, because of irreversible effects inherent to non-equilibrium processes: activation losses arise and Ohmic losses are caused by electric resistance of cell components. In addition, the consumption of reacting species decreases their concentration in the vicinity of reaction sites, leading to a decrease in cell voltage, i.e. concentration losses.

As the cell generates electric power, heat is generated within its components, i.e. electrodes and the electrolyte, as a result of reversible and irreversible effects. All three modes of heat transfer, conduction, convection and radiation, are present in a SOFC occurs.

3.2. Mathematical model

The transport of reactants from the inlet, through the gas channels and then the porous electrodes to the reaction sites had to be modelled, because electrochemical potential and reaction rates depend on the concentration of components. The gas phase momentum and mass transfer were modelled by the compressible Navier–Stokes equation and the Maxwell–Stefan model for multi-component diffusion respectively. Gas flow within the electrodes

Table 1
Model equations except for heat transfer.

Equation	Domains
Overall mass balance (continuity)	
$\nabla \cdot (\rho \mathbf{u}) = \dot{m} \quad \dot{m} = \begin{cases} -\frac{i_{\text{An}}^{\text{gen}}}{2F} (M_{\text{H}_2} - M_{\text{H}_2\text{O}}) & \text{AFL, ASL} \\ \frac{i_{\text{Ca}}^{\text{gen}}}{4F} M_{\text{O}_2} & \text{CFL} \\ 0 & \text{elsewhere} \end{cases}$	Anode gas channel, cathode gas channel, ACCL, ASL, AFL, CFL, CCCL
Navier–Stokes (momentum balance)	
$\rho(\mathbf{u} \cdot \nabla) \mathbf{u} = \nabla \cdot \left[-p\mathbf{I} + \mu(\nabla \mathbf{u} + (\nabla \mathbf{u})^T) - \frac{2}{3}\mu(\nabla \cdot \mathbf{u})\mathbf{I} \right]$	Anode gas channel, cathode gas channel
Darcy's law (momentum balance in porous media)	
$\mathbf{u} = -\frac{\nabla p}{\mu}$	ACCL, ASL, AFL, CFL, CCCL
Species balance	
$\nabla \cdot (\mathbf{N}_i^m) = \dot{m}_i \quad \begin{cases} N_i^m = J_i^m + c_i^m \\ c_i^m = \rho \omega_i \mathbf{u} \end{cases} \quad \dot{m}_i = \begin{cases} -\frac{i_{\text{An}}^{\text{gen}}}{2F} M_i & \text{AFL, ASL} \\ \frac{i_{\text{Ca}}^{\text{gen}}}{4F} M_i & \text{CFL} \\ 0 & \text{elsewhere} \end{cases}$	Anode gas channel, cathode gas channel, ACCL, ASL, AFL, CFL, CCCL
Multi-component mass diffusion (Maxwell–Stefan model)	
$\mathbf{J}_i^m = -\rho \omega_i \sum_{j=1}^n D_{ij} \left(\nabla x_j + (x_j - \omega_j) \frac{\nabla p}{p} \right) \quad \omega_i = \frac{x_i M_i}{\sum_{j=1}^n x_j M_j}$	Anode gas channel, cathode gas channel
Multi-component mass diffusion in porous media (dusty-gas model)	
$\frac{\nabla p_i}{RT} = \sum_{j=1}^n \frac{x_j \mathbf{J}_i - x_i \mathbf{J}_j}{D_{ij}^e} + \frac{\mathbf{J}_i}{D_{ik}^e} \quad \begin{cases} D_{ik} = \frac{2}{3} r_o \sqrt{\frac{8RT}{\pi M_i}} \\ D_{ij}^e = \frac{\varepsilon}{\tau} D_{ij} \\ \tau = (1 - (1 - \varepsilon)^{2/3}) / \varepsilon \end{cases}$	ACCL, ASL, AFL, CFL, CCCL
Electronic charge transfer	
$\nabla \cdot (-\sigma_{\text{elec}}^{\text{eff}} \nabla V_{\text{elec}}) = Q_{\text{elec}} \quad Q_{\text{elec}} = \begin{cases} -i_{\text{gen,An}} & \text{AFL, ASL} \\ -i_{\text{gen,Ca}} & \text{CFL} \\ 0 & \text{elsewhere} \end{cases}$	ACCL, ASL, AFL, CFL, CCCL
Ionic charge transfer	
$\nabla \cdot (-\sigma_{\text{ion}}^{\text{eff}} \nabla V_{\text{ion}}) = Q_{\text{ion}} \quad Q_{\text{ion}} = \begin{cases} i_{\text{gen,An}} & \text{AFL, ASL} \\ i_{\text{gen,Ca}} & \text{CFL} \\ 0 & \text{elsewhere} \end{cases}$	ASL, AFL, electrolyte, CFL

was modelled using Darcy's law, and mass transfer was described by the dusty-gas model. Modelling composite electrodes, electrochemical reactions were assumed to occur within the volume of the electrodes. The Nernst equation and Ohm's law were used to model ionic and electronic potentials and currents within the electrodes and the electrolyte. Reaction rates were calculated using the complete Butler–Volmer equation at each point within the electrodes using the local pressure and composition conditions. Modelling of mass, momentum, and charge transfer as well as the electrochemical reaction kinetics are described in detail in Ref. [59] where the development of an isothermal model is described. Validation experiments were conducted in a three-zone tubular furnace, keeping a uniform temperature along cell's active length. Reaction kinetic constants were estimated for electrodes. The model was successfully validated against experiments, and it was found to be consistent in its description and prediction of the physical reality of the cell. Table 1 gives equations for all of the phenomena except for the heat transfer model.

For the non-isothermal model, equations used for the isothermal model remain essentially unchanged once they account for the temperature dependency of the physical properties and parameters. The buoyancy effect was ignored in the fluid flow model. The diffusion-thermo effects on mass and energy transport, thermal diffusion and Dufour effects, are negligible [60].

3.2.1. Conductive and convective heat transfer

Heat transfer in porous electrodes can be modelled using volume averaged equations, in which the quantities of interest are averaged over a representative elementary volume (REV). A rigorous development of these equations for modelling battery systems is presented elsewhere [61] which can equally be applied to a SOFC porous electrode. Local thermal equilibrium is assumed, which is the case for SOFC electrodes [62]. At steady-state conditions, the general form of the equation for a composite electrode comprising of k phases is:

$$\nabla \cdot (-\bar{\lambda} \nabla T) + \bar{\rho C_p} \cdot \nabla T = q_{\text{h,gen}} \quad (2)$$

The average thermal mass and the average thermal conductivity of the REV, denoted $\bar{\rho C_p}$ and $\bar{\lambda}$ respectively, are calculated as:

$$\bar{\rho C_p} = \sum_k \phi_k \rho_k C_{p,k} \mathbf{u}_k \quad \text{and} \quad \bar{\lambda} = \sum_k (\lambda_k^{\text{eff}} + \lambda_{a,k}).$$

The volume fraction, density, specific heat capacity and velocity of phase k are denoted ϕ_k , ρ_k , $C_{p,k}$, and \mathbf{u}_k . The effective conductivity of phase k , λ_k^{eff} , includes tortuosity effects. The hydrodynamic dispersion, $\lambda_{a,k}$, appears as an artefact owing to the volume averaging of equations. It represents the effect of velocity and temperature

variation within the REV. The volumetric heat source $q_{h,gen}$, includes volumetric and interfacial heat generation within the REV.

The gas phase contribution to heat transfer in the porous electrodes is quite small compared to the solid phase, because of the relatively small heat capacity and thermal conductivity of the gas. In the solid phase, $\lambda_{a,k}$ is zero by definition. Therefore, for the porous electrode, equation (2) simplifies to:

$$\nabla \cdot (-\lambda_{solid}^{eff} \nabla T) = q_{h,gen} \quad (3)$$

The effective thermal conductivity of the solid phase is λ_{solid}^{eff} . The heat transported by the flow of oxygen ions, the ionic current, can be included in the model [63]; but it is negligible because the Thomson coefficient, equivalent to the heat capacity, of oxygen ions in YSZ is half that of oxygen gas [64]. It can be neglected if the convection of oxygen gas can be neglected.

The total volumetric heat generation, $q_{h,gen}$, includes the reversible and irreversible heating effects. The reversible heat originates from the electrochemical half-reactions entropy change. The irreversible heating is caused by Ohmic losses within electric current conductors, and by the irreversibility of electrochemical reactions which occurs away from equilibrium, i.e. the activation overpotential. Note that while there is no irreversible heat generation in an ideal fuel cell, reversible heating is always present, even for an ideal cell. The volumetric irreversible heat source, $q_{h,irr}$, is calculated as:

$$q_{h,irr} = \sigma_{ionic}^{eff} \nabla V_{ionic} \cdot \nabla V_{ionic} + \sigma_{elec}^{eff} \nabla V_{elec} \cdot \nabla V_{elec} + i_{gen} \eta_{act} \quad (4)$$

The first two terms on the RHS represent ionic and electronic charge conduction resistive heating, while the third term represents heating due to activation overpotential.

The reversible heat generation of a single-electrode at each point in the electrode volume was calculated using local temperature, pressure, and composition. The full cell heat of reaction is straightforward to calculate based on thermodynamic relations; however, its calculation is more involved for half-reactions. Without giving the details, the expressions for calculating half-reaction reversible heat

generation, accounting for temperature and concentration dependence, are presented here, which were derived based on transported entropy of oxide ions and electrons. Oxygen reaction entropy change was estimated based on its Seebeck coefficient.

The volumetric reversible heat generation within the cathode and anode is calculated as:

$$q_{h,cathode}^{rev} = \frac{-i_{gen}}{2F} \left(-T \Delta S_{cathode}(T, p_{O_2}^0) \right) = \frac{i_{gen} T}{2F} \left(-89.3 + \frac{R}{2} \ln \left(\frac{p_{O_2}}{1 \times 10^5} \right) \right) \quad (5)$$

$$q_{h,anode}^{rev} = i_{gen} \left(-T \Delta S_{anode}(T, p_{O_2}^0) \right) = -\frac{i_{gen} T}{2F} \left(\Delta S_{cell}(T, p_i^0) + R \ln \left(\frac{p_{H_2}}{p_{H_2O}} \right) + 89.3 \right) \quad (6)$$

The entropy change of the overall reaction at standard pressure, $\Delta S_{cell}(T, p_i^0)$, can be calculated from standard thermodynamic relations, as presented in [Appendix](#). The rate of volumetric electron generation is denoted i_{gen} .

3.2.2. Radiative heat transfer

Radiation between the surfaces of anode and cathode electrodes and gas channels was modelled, while gases were assumed to be transparent to radiation, i.e. no gas absorption. Note that the self-radiation between the convex surfaces was captured by this model. The net radiative flux at point (x) on a surface, q_{net}^r , is the balance of the outgoing and incoming fluxes, i.e. radiosity (q_{out}^r) and irradiation (q_{in}^r):

$$q_{net}^r(x) = q_{out}^r(x) - q_{in}^r(x) \quad (7)$$

The radiosity of an opaque, grey, diffuse surface is the sum of emitted and reflected radiation:

$$q_{out}^r(x) = \varepsilon \sigma (T(x))^4 + (1 - \varepsilon) q_{in}^r(x) \quad (8)$$

The emissivity, ε , is a function of temperature, and σ is the Stefan–Boltzmann constant.

Table 2
Electric conductivity of the solids.

Electric conductivity (S m ⁻¹)	
Anode support, effective electronic (σ_{elec}^{eff}) [†] Experimental ^{††} By Ref. [72]	$\frac{3.77 \times 10^{47}}{T} e^{-\frac{115011}{T}}$
Anode functional, effective electronic (σ_{elec}^{eff}) [†] Experimental ^{††} By Ref. [72]	$\frac{2.17 \times 10^{77}}{T} e^{-\frac{115011}{T}}$
Cathode functional, effective electronic (σ_{elec}^{eff}) (Experimental)	$\frac{6.10 \times 10^6}{T} e^{-\frac{3350}{T}}$
Anode/cathode functional, effective ionic (σ_{elec}^{eff}) [†] By Ref. [59] ^{††} By Ref. [72]	$1.15 \times 10^{47} e^{-\frac{1030011}{T}}$
Anode support, effective ionic (σ_{elec}^{eff}) [†] By Ref. [59] ^{††} By Ref. [72]	$9.53 \times 10^{37} e^{-\frac{1030011}{T}}$
Electrolyte [72]	$3.34 \times 10^4 e^{-\frac{10300}{T}}$
Gold, fitted [73]	$\frac{1}{9.22 \times 10^{-11} T - 5.3710^{-9}}$
Nickel [74]	$\log(\sigma) = 8.2475 - 4.9 \times 10^{-3} T + 4 \times 10^{-6} T^2 - 1 \times 10^{-5} T^3$

T in (K).

Table 3
Temperature dependent kinetic parameters.

Reaction kinetics; volumetric electron generation (A m^{-3})	
Anode [75]	$i_{\text{gen,An}} = i_{0,\text{An}} \left(e^{\frac{1.5F}{RT} \eta_{\text{An}}} - e^{-\frac{0.5F}{RT} \eta_{\text{An}}} \right)$
[†] Experimental	$\eta_{\text{An}} = V_{\text{elec,An}} - V_{\text{ion,An}} - \varepsilon_{\text{An}}$
^{††} By Ref. [75]	$i_{0,\text{An}} = i_{s,\text{An}} \frac{(p_{\text{H}_2}/p_{\text{H}_2}^*)^{1/4} (p_{\text{H}_2\text{O}})^{3/4}}{1 + (p_{\text{H}_2}/p_{\text{H}_2}^*)^{1/2}}$
	$p_{\text{H}_2}^* = 1.22 \times 10^8 T^{1/2} e^{-\frac{88,120}{RT}}$
	$i_{s,\text{An}} = 5.08 \times 10^{13} i e^{-\frac{88,120}{RT}}$
Cathode [75]	$i_{\text{gen,Ca}} = i_{0,\text{Ca}} \left(e^{\frac{0.5F}{RT} \eta_{\text{Ca}}} - e^{-\frac{0.5F}{RT} \eta_{\text{Ca}}} \right)$
[†] Experimental	$\eta_{\text{Ca}} = V_{\text{elec,Ca}} - V_{\text{ion,Ca}} - \varepsilon_{\text{Ca}}$
^{††} Experimental, 200,000 by Ref. [75]	$i_{0,\text{Ca}} = i_{s,\text{Ca}} \frac{(p_{\text{O}_2}/p_{\text{O}_2}^*)^{1/4}}{1 + (p_{\text{O}_2}/p_{\text{O}_2}^*)^{1/2}}$
	$i_{s,\text{Ca}} = 1.47 \times 10^{15} i e^{-\frac{128,000}{RT}}$

T in (K).

The irradiation at any point (x), is the sum of radiative heat flux arriving to a point from every other point (ξ) on the surrounding surfaces (Γ).

$$q_{\text{in}}^r = \int_{\Gamma} q_{\text{out}}^r(\xi) \theta(x, \xi) \omega(x, \xi) d\xi \quad (9)$$

where ω is a geometric factor accounting for the effect of surfaces' relative orientation on the radiative power exchanged, and θ is the visibility factor:

$$\omega(x, \xi) = \frac{-(\mathbf{r} \cdot \mathbf{n}_x)(\mathbf{r} \cdot \mathbf{n}_\xi)}{\pi |\mathbf{r}|^4}, \quad \theta(x, \xi) = \begin{cases} 1 & x \text{ and } \xi \text{ see each other} \\ 0 & \text{otherwise} \end{cases} \quad (10)$$

where \mathbf{r} is the vector connecting the two points, and \mathbf{n} is the vector normal to surface.

Equations (9) and (10) form a set of integro-differential equations, the radiosity equation [65], that models radiative exchange in an enclosure. The effect of radiation is included in the model through equation (8) as a boundary condition.

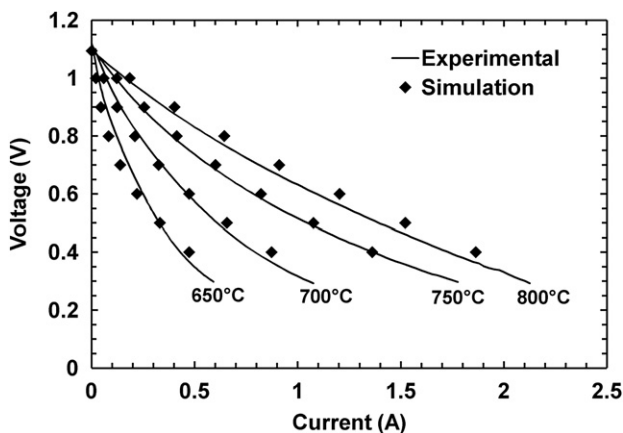


Fig. 4. The overall performance prediction of the cell at various temperatures and the experimental results.

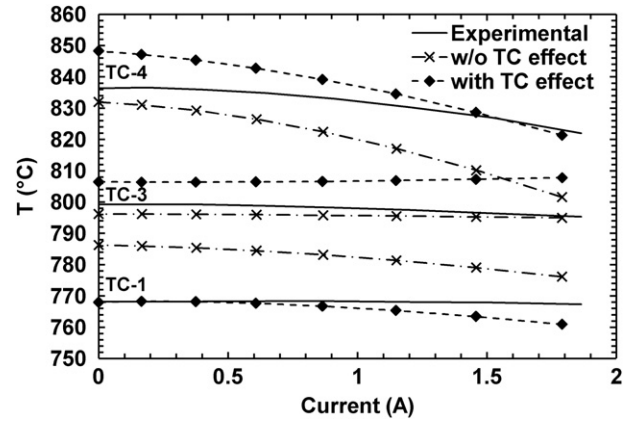


Fig. 5. The temperature distribution prediction within the furnace versus the experimental.

3.2.3. Electromotive force of a non-isothermal electrochemical cell

The electromotive force (EMF) of non-isothermal anode and cathode can be calculated as:

$$\begin{aligned} -2F(-\varepsilon_{\text{anode}}(T, p_{\text{H}_2}, p_{\text{H}_2\text{O}})) &= \Delta G_{\text{cell}}(T, p_i^0) + RT \ln \left(\frac{p_{\text{H}_2\text{O}}}{p_{\text{H}_2}} \right) \\ &\quad - (T^0 - T) \Delta S_{\text{Cathode}}(p^0) \end{aligned} \quad (11)$$

$$\begin{aligned} -2F(-\varepsilon_{\text{cathode}}(T, p_{\text{O}_2})) &= \frac{RT}{2} \ln \left(\frac{p_{\text{O}_2}}{p_{\text{O}_2}^0} \right) - (T^0 - T) \Delta S_{\text{Cathode}}(p^0) \end{aligned} \quad (12)$$

4. Model implementation and solution

The model equations form a set of nonlinear interdependent differential equation that had to be solved simultaneously, with proper boundary conditions. Taking advantage of the axial symmetry of the system, the equations were solved on a 2-dimensional domain, see Fig. 3.

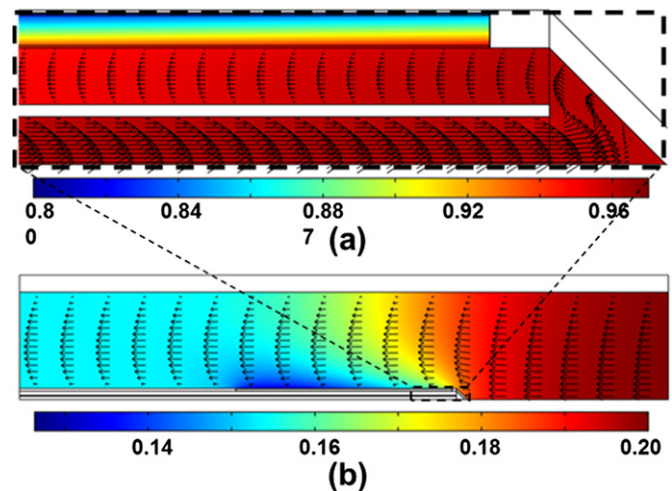


Fig. 6. The simulated concentration distribution and the velocity profile: (a) the hydrogen mole fraction on the anode side; (b) the oxygen mole fraction on the cathode side. The arrows show (a) the hydrogen, and (b) the air velocity profile.

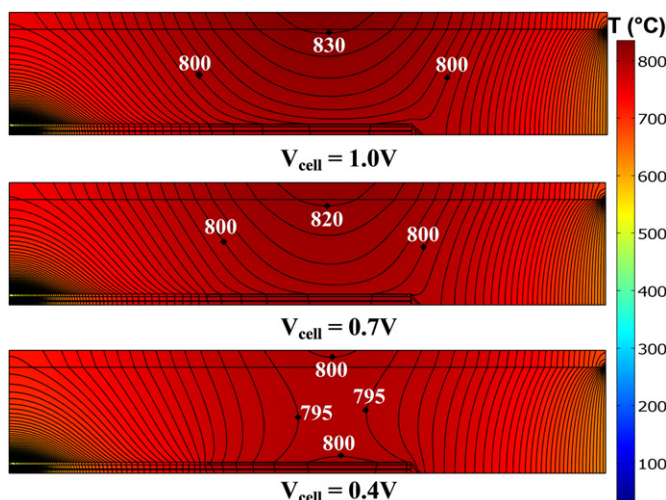


Fig. 7. The predicted temperature distribution at various cell voltages. Adjacent contours are 5 °C apart.

4.1. Boundary conditions

The boundary conditions for heat transfer model are explained here; the rest are described elsewhere [59]. A Dirichlet boundary condition was used at the inlet of air and fuel gas channels, prescribing the inlet temperature of the air and fuel side. Experiments showed that air was preheated before entering the system, due to the relatively low air velocity. Therefore the inlet temperature of air was set to 625 °C, based on experimental measurements (TC-5 in Fig. 3). Hydrogen inlet temperature was assumed to be 25 °C, as it entered the system with high velocity.

A convection boundary condition was assumed on the gas channel outlet. A constant inward heat flux was assumed along the outer surface of the furnace, representing the effect of the electric heating coil. Surface to surface radiation was implemented as a heat sink on solid/gas boundaries. Zero flux was implemented along the geometry's axis of symmetry. Continuity of temperature and conductive heat flux was assumed on all other boundaries within the system.

4.2. Model parameters

The model parameters included thermo-physical properties and kinetic parameters, which were calculated using appropriate local

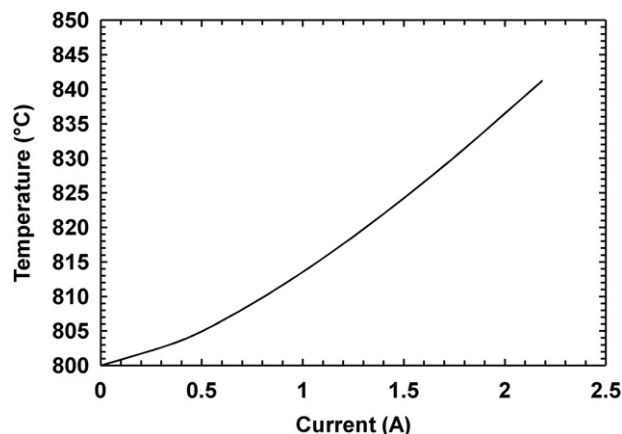


Fig. 9. The temperature of the middle of the active length (TC-2) at constant furnace heat flux, as a function of cell current load.

conditions, i.e. pressure, temperature, and concentration. Expressions to estimate the thermo-physical properties, i.e. heat capacities of pure components, enthalpy, entropy, and Gibbs free energy change of reaction, thermal conductivity of gases and solids, and emissivity of solids are presented in Appendix.

Reaction kinetic constants for each electrode are critical for the accuracy of the model predictions. In our previous work [59], reaction kinetic parameters were estimated for an isothermal cell based on experimental results conducted at isothermal conditions in a three-zone furnace. For this study, Arrhenius type functions were used to capture the temperature dependence of reaction kinetic constants from our previous isothermal estimates. The values are shown in Table 2. The exponential constant (activation energy, E_a) of the cathode kinetic expression was estimated experimentally based on electrochemical impedance spectroscopy (EIS) of symmetric electrodes on button cell samples, while a value reported in the literature was used for the anode. The latter would be an extrapolation and a potential source of error in model predictions. However, it was concluded in our previous study [59] that the anode was significantly more active compared to the cathode and therefore had a negligible contribution to the overall cell performance loss. Therefore extrapolating the anode kinetic parameter's temperature dependence using E_a from the literature – instead of experimental measurement – was not expected to introduce a significant error in cell performance predictions.

The temperature-dependent effective electronic conductivity of the cathode layer was also estimated experimentally [59]. The

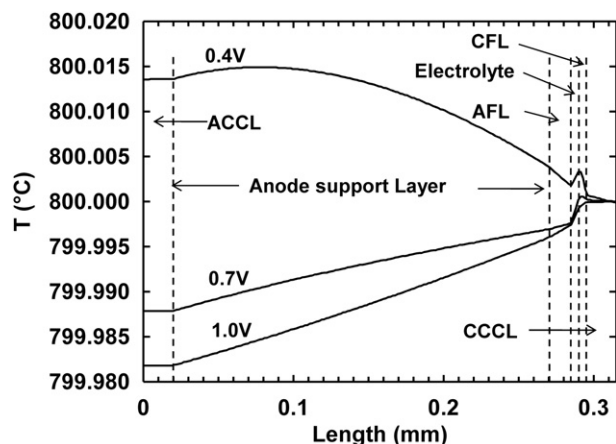


Fig. 8. The temperature distribution within the cell layers in the radial cross section at the middle of the active length.

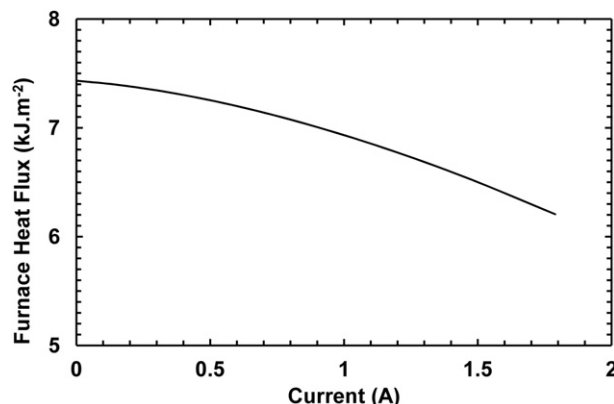


Fig. 10. The estimated furnace heat flux at various current loads.

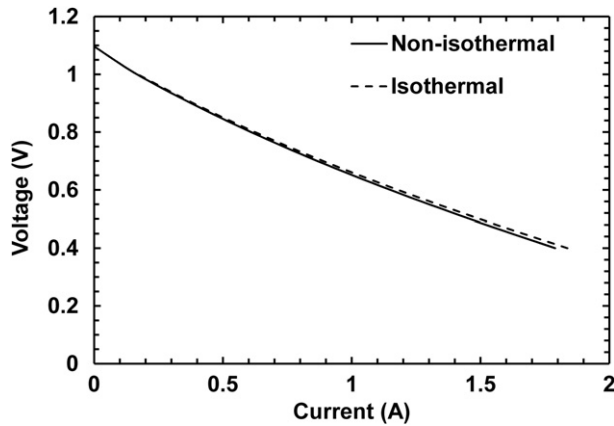


Fig. 11. The overall performance curves predicted by the isothermal model and the non-isothermal model.

temperature dependent electric conductivities of solids are shown in Table 3. The effective electronic conductivity of anode support and anode functional layer was extrapolated from the values estimated in our 800 °C isothermal experiments, using the activation energy for nickel obtained from the literature.

The fuel and air flow rates were 50 and 100 mL s⁻¹ at STP for experiments and the model. Hydrogen was passed through a bubbler at room temperature which added about 3% humidity to the fuel side.

4.3. Geometry discretization

The model geometry was discretized as shown in Fig. 3. A structured multi-scale mesh was used to discretize the domain, as there was a significant length-scale difference within modelled domains, from the micron thin electrodes to centimetre wide gas channels. The mesh had 40 nodes in the cross section of the air channel, the diffuser tube, and the annular space between the diffuser and the cell. It had 320 nodes along the active length of the cell and total number of 480 nodes along the furnace. Forty nodes were used to resolve the cross section of each layer of the active length. The mesh was finer where steeper change was expected, i.e. close to the walls, as well as at the electrode/electrolyte interface where most of the electrochemical reactions were expected to occur. Using a structured mesh drastically reduced the computational demand of the numerical scheme. In addition, the convergence was faster and much smoother due to alignment of transport fluxes with the mesh. By successive systematic refinements of the mesh, it was ensured that the solution was mesh-independent and the number of nodes described above reflects this mesh.

4.4. Equation discretization

The model equations formed a system of coupled non-linear equations. A commercial finite element solver, COMSOL, was used to solve the equations on the 2D axi-symmetric domain. Second order Lagrangian polynomials were used to discretize and

approximate the solution on the numerical grid (first order elements for pressure).

Axial symmetry does not readily simplify three dimensional radiation heat transfer equation, unlike transport equations, down to two dimensions. Despite this, symmetry has been occasionally used for the radiation model [36,51] which would imply inaccuracies of unknown magnitude. The complete geometry of our model was generated by rotating the 2D domain around its axis of symmetry in 128 azimuthal sectors. The radiosity equation was discretized on the resulting mesh into surfaces that exchange radiation with each other [66]. View factors between the surface elements were then calculated based on the hemi-cube method [67]. The hemi-cube method is commonly used in computer graphics to render geometrically complex environments, and can effectively handle the effect of objects blocking each other out. View factors are calculated once and for all at the beginning of the solution. The resulting discretized radiosity equation is linear in terms of the radiosity, which should be simultaneously solved with the rest of the model.

4.5. Numerical solution

The discretized equations were solved using Newton's iterative method, with a direct solver, UMFPACK. Computations were performed on 16 Quad-Core AMD Opteron 8274 CPU equipped with 66 GB of RAM.

As the system of equations were highly non-linear, an appropriate solution strategy and a suitable initial solution were essential for obtaining the numerical solution. The solution was first obtained for an "isothermal" model, where all equation variables were solved for except for the heat transfer model, while the temperature of the entire domain was fixed at the temperature of the middle of the active length (TC-2). Next, using the isothermal solution as the initial condition, the full model including heat transfer was solved. The solution strategy for the isothermal model, to have a guaranteed and stable numerical convergence, is explained in detail in Ref. [59]. The furnace heat flux, however, was unknown and had to be found such that the temperature of the middle of the active length (TC-2) was equal to the desired value. This was done by solving a function that obtained a solution for the non-isothermal model, and had furnace heat flux as its input variable and TC-2 as its output variable; Newton's method was used to find the solution for the heat flux.

5. Results and discussions

The model was numerically solved to obtain temperature, velocity, and concentration profiles within gas channels and porous electrodes, and electrochemical reactions within electrodes. We focus on the thermal aspect of the model here.

5.1. Experimental validation

The model predictions were compared to experimental results in two aspects: the overall cell performance, and the temperature distribution within the system. As mentioned before, no parameter

Table 4
The polynomial coefficients of the pure component heat capacity correlation [70].

	b_0	b_1	b_2	b_3	b_4	b_5	b_6	Error %	C_p (1473 K)
H ₂	21.157	56.036	-150.55	199.29	-136.15	46.903	-6.4725	1	32.146
H ₂ O	37.373	-41.205	146.01	-217.08	181.54	-79.409	14.015	1	46.831
N ₂	29.027	4.8987	-38.04	105.17	-113.56	55.554	-10.35	1	34.756
O ₂	34.85	-57.975	203.68	-300.37	231.72	-91.821	14.776	1	36.469

Table 5The polynomial coefficients of the ΔH_{rxn} and ΔS_{rxn} correlation polynomials.

	b_0	b_1	b_2	b_3	b_4	b_5	b_6	b_7
ΔH_{rxn}	−239,706	−1.209	−34.1268	64.90667	−66.54625	40.366	−13.4003	1.871357
ΔS_{rxn}	−32.1487	−68.2535	97.3600	−88.72833	50.4575	−16.0803	2.183250	−1.209

fitting was done for this model; all the parameters were obtained experimentally or from the literature, and the kinetic parameters estimated in our previous paper for an isothermal system at 800 °C. Therefore all the results presented here are completely predictive.

The overall cell performance predicted by the model at various temperatures is compared to the experimental results in Fig. 4. Good agreement between the predictions and the experimental data is seen.

The predicted temperature distribution is compared to the experimental in Fig. 5. As the three thermocouple rods attached to the cell had a thickness comparable to the $T\mu$ SOFC's very thin wall, they influenced the temperature distribution around the cell within the furnace. The thermocouple rods enhanced the thermal conduction along the cell, acting similar to a thermal fin. The thermocouples could not be included in our 2D axi-symmetric model because they violated the axial symmetry, requiring a full 3D simulation. Therefore the influence of the thermocouples on the axial thermal conduction was accounted for by artificially enhancing the thermal conductivity of the anode support layer in the axial direction. Fig. 5 shows that including the effect of thermocouple rods did somewhat improve temperature distribution predictions overall. Therefore the thermocouples did noticeably affect the thermal distribution within the furnace. A similar effect has been reported to occur within monolith reactors, where the fin effect of the thermocouple rods interfered with the temperature readings [68]. With or without the thermocouple effect, temperature distribution predictions are relatively consistent with the experimental in terms of their relative magnitude (i.e. TC-4 > TC-3 > TC-1). Also, consistent with the experimental, the model predicts TC-4 to have the highest changes of temperature versus current generation, quite larger than TC-3 and TC-1. As we were interested in the behaviour of the cell itself, all the subsequent results are reported for the model that does not include the effect of thermocouples. Another noteworthy aspect of Fig. 5 is an overall decrease in the active length temperature when current is increased. This is because the cell heat generation contributes more to keeping TC-2 at 800 °C, hence furnace has to provide less heat flux. As a result, the system becomes cooler while TC-2 remains at 800 °C.

5.2. Gas flow and concentration distribution

Fig. 6 shows the mole fraction of hydrogen and oxygen within their respective gas channels. Hydrogen and oxygen were consumed as the flow passed the active length of the cell, and their concentrations decreased. Note that the velocity profile within the gas channels is shown by arrows, which are normalized within their own gas channel. The velocity in the fuel cell tube was much higher than the velocity in the air channel.

Table 6

Thermal conductivity of the solids.

Thermal conductivity of solids ($W K^{-1} m^{-1}$)	
Cathode, effective [53]	6
Anode, effective [53]	11
YSZ [53]	2.7
Gold [76]	$-0.0583T + 336.08$
Alumina [76]	$3.6919e^{\frac{-668.71}{T}}$

T in (K).

Table 7

Specific heat capacity of the solids.

Specific heat capacity ($J kg^{-1}$)	
LSM [77]	573
Nickel ^a	$293 + 0.496T \quad T < 630 K$ $489 + 0.0617T \quad T > 630 K$
YSZ ^a	$686 - \frac{6.91 \times 10^4}{T}$
Gold ^a	$145 - 2.62 \times 10^{-2}T + 4.15 \times 10^{-5}T^2$
Alumina ^a	$1413.6 - \frac{189,613}{T}$

T in (K).

^a Ref. [78].

5.3. Temperature distribution within gas channels and cell layers

The predicted temperature profile within the furnace and the $T\mu$ SOFC for a range of cell voltages is shown in Fig. 7; a lower voltage corresponds to a higher current load, as was shown in Fig. 4. It is clear that the temperature profile has a complex pattern, completely changing with the current load. At a low current load, only the furnace contributes to the heating of the system. The maximum temperature occurs around the middle of the furnace tube. At a high current load however, the shape of the temperature profile changes around the active length, and has a maximum close to the middle of the active length. This occurs because of the significant heat released by the electrochemical reactions occurring within the active length of the cell. As was explained for Fig. 5, this results in the system overall being cooler, as the furnace is putting in less heat to keep TC-2 at 800 °C. The temperature gradients along the cell's active length tend to increase at higher current loads, but are always less than about 25 °C (which was at 0.4 V). Note that the middle of the active length, which corresponds to TC-2 being kept at 800 °C by the furnace controller. The temperature decreases towards the outlet mainly due to the thermal radiation lost to the ambient, through the open end of the furnace.

The temperature within the electrode and the electrolyte increases because of the heat generation. It is of practical importance to know the magnitude of this temperature rise, and whether it is within the acceptable range. The temperature profile across the active length is shown in Fig. 8, distinguishing the several cell layers. Note that the temperature difference within the thickness of the active length is less than 0.015 °C, even at the highest current load. The temperature profile slightly peaks at the cathode/electrolyte interface, where most of the heat is generated. The temperature has a relatively flat peak within the anode support layer at the high current load, resulting from the ohmic heating due to its lower than usual electronic conductivity [59]. The temperature within current collectors is very flat, due to the very high thermal conductivity of gold.

Fig. 9 provides an important practical insight into the cell's operation, estimating cell temperature increase due to its operation

Table 8

Emissivity of the solids.

Emissivity of solids	
All components	0.7 [24]; 0.9 [63]
Alumina	0.5 (1073 K) [78]

Table 9

The polynomial coefficients of the pure component thermal conductivity correlation.

	b_0	b_1	b_2	b_3	b_4	b_5	b_6	Error %	κ (1473 K)
H ₂	1.504	62.892	−47.19	47.763	−31.939	11.972	−1.8954	5	57.705
H ₂ O	2.0103	−7.9139	35.922	−41.39	35.993	−18.974	4.1531	1	16.303
N ₂	−0.3216	14.81	−25.473	38.837	−32.133	13.493	−2.2741	5	9.4124
O ₂	−0.1857	11.118	−7.3734	6.713	−4.1797	1.491	−0.2278	10	9.9832

while the furnace heat flux is constant. The initial temperature of the middle of the active length (TC-2) was 800 °C when no current was drawn from the cell. With the furnace heat flux held constant, the temperature rose by about 40 °C when ~ 2 A (corresponding to $V_{\text{cell}} = 0.4$) current was drawn from the cell.

Heat should be always provided to the system to keep it at its operating temperature, as the numerically estimated furnace heat flux is always positive; see Fig. 10. These values should be lower than real values, as in reality the furnace tube loses heat to the environment despite the insulation around it. The trend shows that at higher current loads, when the cell is generating more heat, less heat flux has to be provided by the furnace. Another insight from Fig. 10 is the fact that the effect of cell heating even at the highest load can account for just about 17% of furnace's load (6.2 kJ m^{-2} compared to 7.4 kJ m^{-2}), indicating the significant role of the furnace for maintaining appropriate operating conditions for single-cell tests.

5.4. Comparison of performance curves for isothermal and non-isothermal conditions

The performance predictions of the isothermal system at 800 °C and the non-isothermal system (where only the middle of the active length was kept at 800 °C) are compared in Fig. 11. For the particular setup and conditions of this system, an isothermal model predicted the cell overall performance quite accurately compared to the complete non-isothermal model with the only the middle of the active length kept at 800 °C. This observation is consistent with a previous modelling study concluding that isothermal models can be acceptably used for the overall performance prediction [69]. In our case, this indicates that overall, temperature variations do not significantly affect current generation in our particular cell/setup. Considering the temperature profile along the active length (Fig. 6) and the performance sensitivity to temperature (Fig. 4), this could be because of the fact that some parts of the active length end up hotter and some parts cooler than 800 °C, cancelling each other out. It has to be reiterated that this observation is valid for the particular setup of this study, cannot be generalized without extreme care, and in fact most likely expected to be not the case for other scenarios. Nevertheless, this observation is a significant knowledge from a computational point of view for conducting further optimization studies on the TμSOFC single cell geometry under the particular circumstances of this study: the isothermal model for each I – V point takes only few minutes to converge to a solution compared to the several hours for the non-isothermal simulation. This scenario, only and only when appropriate for example for the very particular setup and conditions of the system modelled in this work, leads to a tremendous reduction in the required computational load and time for optimization studies by using an isothermal model instead of a full non-isothermal model, without compromising the usefulness of the I – V data collected on the non-isothermal setup with the middle of the active length kept at a constant temperature.

6. Conclusion

A detailed non-isothermal model was developed for a TμSOFC. The model predictions were found to be consistent with the

experimental results on the cell overall performance as well as temperature distribution. The temperature profile was found to be a complex outcome of various effects, especially radiation. Had the furnace heat flux remained constant, the heat generated by the cell could raise its temperature as much as 40 °C.

In a setup in which the middle of the active length is kept at constant temperature, the prediction of the cell overall performance by the isothermal model was very close to the non-isothermal model. This result is useful for the particular conditions described in this work, which represents a typical experimental single TμSOFC testing setup. Because single-cell studies are the first step towards developing cells and stacks, this insight be quite helpful: using a single-zone furnace, under the particular conditions studied here, the experimentalist does not need to be concerned with non-isothermal effects on electrochemical performance results.

Acknowledgements

This work was financially supported by Alberta Ingenuity Fund in Nanotechnology, and Natural Science and Engineering Council of Canada (NSERC) strategic grant.

Appendix

The gas mixture heat capacity

The specific mass heat capacity of an ideal gas mixture, \bar{C}_p , can be calculated as a function of its composition as:

$$\bar{C}_p(T) = \sum_{\text{species}} \omega_i \frac{C_{p,i}(T)}{M_i} \quad (13)$$

where M_i and ω_i are the molecular mass (kg mol^{-1}) and mass fraction of component i . The specific molar heat capacity of a pure component, $C_{p,i}$, can be calculated as a polynomial function of temperature [70]:

$$C_p(T) = \sum_{i=0}^6 b_i \left(\frac{T}{1000} \right)^i \quad (14)$$

where C_p has units of ($\text{J mol}^{-1} \text{K}^{-1}$) and T is in (K). The coefficients in equation (14), b_i , are listed in Table 4.

The reaction enthalpy, entropy, and Gibbs free energy change

The specific enthalpy change (ΔH_{rxn}) and specific entropy change (ΔS_{rxn}) of the overall chemical reaction ($\text{H}_2 + 0.5\text{O}_2 \rightarrow \text{H}_2\text{O}$) at any given temperature, assuming ideal gas conditions, can be calculated as:

$$\begin{aligned} \Delta H_{\text{rxn}}(T) &\equiv H_{\text{H}_2\text{O}}(T) - H_{\text{H}_2}(T) - \frac{1}{2} H_{\text{O}_2}(T) \\ &= \Delta H_{\text{rxn}}(T^\circ) + \int_{T^\circ}^T \Delta C_{p,\text{rxn}}(\tau) d\tau \end{aligned} \quad (15)$$

$$\begin{aligned}\Delta S_{\text{rxn}}(T, p^0) &\equiv S_{\text{H}_2\text{O}}(T, p^0) - S_{\text{H}_2}(T, p^0) - \frac{1}{2} S_{\text{O}_2}(T, p^0) \\ &= \Delta S_{\text{rxn}}(T^0, p^0) + \int_{T^0}^T \frac{\Delta C_{\text{P,rxn}}(\tau)}{\tau} d\tau\end{aligned}\quad (16)$$

where

$$\Delta C_{\text{P,rxn}} = C_{\text{P,H}_2\text{O}} - C_{\text{P,H}_2} - 0.5C_{\text{P,O}_2}.$$

Using equations (15) and (16), and considering $\Delta H_{\text{rxn}}^0 = -241,820 \text{ (J/mol}^{-1}\text{)}$ and $\Delta S_{\text{rxn}}^0 = -44.37 \text{ (J mol}^{-1} \text{K}^{-1}\text{)}$ at standard conditions (25 °C and 1 bar) [71], the following working expressions can be obtained:

$$\Delta H_{\text{rxn}}(T) = \sum_{i=0}^7 b_i \left(\frac{T}{1000} \right)^i \quad (17)$$

$$\Delta S_{\text{rxn}}(T, p_i = 1 \text{ bar}) = \sum_{i=0}^6 b_i \left(\frac{T}{1000} \right)^i + b_7 \ln \left(\frac{T}{1000} \right) \quad (18)$$

where ΔH_{rxn} has units (J mol⁻¹) and ΔS_{rxn} (J mol⁻¹ K⁻¹). Both are based on 1 mol of hydrogen consumed. T is the absolute temperature (K). The coefficients for equations (17) and (18) are given in Table 5.

The specific Gibbs free energy change of reaction (ΔG_{rxn}) at any temperature and standard pressure can be simply calculated as:

$$\Delta G_{\text{rxn}}(T, p_i = 1 \text{ bar}) = \Delta H_{\text{rxn}}(T) - T \Delta S_{\text{rxn}}(T, p_i = 1 \text{ bar}) \quad (19)$$

The thermal conductivity of solids

The thermal conductivities of the solids used in this work are given in Table 6.

The specific heat capacity of solids

The heat capacities of solids used in this work are given in Table 7.

The emissivity of solids

The emissivity of the solids used in this work is given in Table 8.

The gas mixture thermal conductivity

The average thermal conductivity, $\bar{\kappa}$, of a gas mixture can be calculated based on the equations developed by Wassiljew [70]:

$$\bar{\kappa} = \frac{\sum_{i=1}^n x_i \kappa_i}{\sum_{j=1}^n x_j B_{ij}} \quad (20)$$

$$B_{ij} = \frac{\left[1 + \left(\frac{\mu_i M_j}{\mu_j M_i} \right) \left(\frac{M_i}{M_j} \right)^{1/4} \right]^2}{[8(1 + M_i/M_j)]^{1/2}} \quad (21)$$

where μ_i and M_i are respectively the dynamic viscosity and the molar mass of the component i .

The thermal conductivity of a pure gas, κ (W m⁻¹ K⁻¹), can be calculated as [70]:

$$\kappa = 0.01 \sum_{i=0}^6 b_i \left(\frac{T}{1000} \right)^i \quad (22)$$

where T is in the absolute temperature (K). The polynomial coefficients for each component, b_i , are listed in Table 9.

References

- [1] I. Zinovik, D. Poulikakos, *Electrochimica Acta* 54 (2009) 6234–6243.
- [2] J. Park, J. Bae, *Journal of Fuel Cell Science and Technology* 8 (2011) 061016.
- [3] J. Park, Y.-M. Kim, J. Bae, *International Journal of Hydrogen Energy* 36 (2011) 3167–3178.
- [4] E. Vakouftsi, G. Marnellos, C. Athanasiou, F.A. Coutelieris, *Chemical Engineering Research and Design* 89 (2011) 224–229.
- [5] M. Ni, *International Journal of Energy Research* 34 (2010) 1027–1041.
- [6] J. Shi, X. Xue, *Electrochimica Acta* 55 (2010) 5263–5273.
- [7] J. Shi, X. Xue, *Journal of Fuel Cell Science and Technology* 8 (2011) 011005.
- [8] A.K. Sleiti, *Journal of Power Sources* 195 (2010) 5719–5725.
- [9] W. Xia, Y. Yang, Q. Wang, *Journal of Power Sources* 194 (2009) 886–898.
- [10] K. Sudaprasert, R.P. Travis, R.F. Martinez-Botas, *Journal of Fuel Cell Science and Technology* 7 (2010) 011002.
- [11] J. Yuan, Y. Huang, B. Sundén, W.G. Wang, *Heat and Mass Transfer* 45 (2009) 471–484.
- [12] Y. Yang, G. Wang, H. Zhang, W. Xia, *Journal of Power Sources* 177 (2008) 426–433.
- [13] Y.N. Magar, R.M. Manglik, *Journal of Fuel Cell Science and Technology* 4 (2007) 185.
- [14] Y. Wang, F. Yoshida, T. Watanabe, S. Weng, *Journal of Power Sources* 170 (2007) 101–110.
- [15] P. Yuan, S.-F. Liu, *Numerical Heat Transfer, Part A: Applications* 51 (2007) 941–957.
- [16] Y. Ji, K. Yuan, J.N. Chung, Y.-C. Chen, *Journal of Power Sources* 161 (2006) 380–391.
- [17] T. Tanaka, Y. Inui, A. Urata, T. Kanno, *Energy Conversion and Management* 48 (2007) 1491–1498.
- [18] B. Morel, J. Laurencin, Y. Bultel, F. Lefebvre-Joud, *Journal of The Electrochemical Society* 152 (2005) A1382.
- [19] Y.X. Lu, L. Schaefer, P.W. Li, *Journal of Fuel Cell Science and Technology* 2 (2005) 65–69.
- [20] Y.P. Chyou, T.D. Chung, J.S. Chen, R.F. Shie, *Journal of Power Sources* 139 (2005) 126–140.
- [21] B.A. Haberman, J.B. Young, *International Journal of Heat and Mass Transfer* 47 (2004) 3617–3629.
- [22] T. Ackmann, L.G.J. de Haart, W. Lehnert, D. Stolten, *Journal of The Electrochemical Society* 150 (2003) A783–A789.
- [23] J. Yuan, M. Rokni, B. Sundén, *International Journal of Heat and Mass Transfer* 46 (2003) 809–821.
- [24] F. Calise, M.D. d'Accadia, G. Restuccia, *International Journal of Hydrogen Energy* 32 (2007) 4575–4590.
- [25] S.M. Jafarian, P. Haseli, G. Karimi, *International Journal of Energy Research* 34 (2010) 946–961.
- [26] S. Hosseini, S.M. Jafarian, G. Karimi, *International Journal of Energy Research* 35 (2011) 259–270.
- [27] J. Jia, R. Jiang, S. Shen, A. Abudula, *AIChE Journal* 54 (2008) 554–564.
- [28] T.W. Song, J.L. Sohn, J.H. Kim, T.S. Kim, S.T. Ro, K. Suzuki, *Journal of Power Sources* 142 (2005) 30–42.
- [29] A.C. Burt, I.B. Celik, R.S. Gemmen, A.V. Smirnov, *Journal of Power Sources* 126 (2004) 76–87.
- [30] M. Ni, *Energy Conversion and Management* 51 (2010) 714–721.
- [31] J. Li, Y.-w. Kang, G.-y. Cao, X.-j. Zhu, H.-y. Tu, J. Li, *Journal of Zhejiang University SCIENCE A* 9 (2008) 961–969.
- [32] J.X. Jia, A. Abudula, L.M. Wei, R.Q. Jiang, S.Q. Shen, *Journal of Power Sources* 171 (2007) 696–705.
- [33] P.W. Li, L. Schaefer, M.K. Chyu, *Journal of Heat Transfer-Transactions of the ASME* 126 (2004) 219–229.
- [34] M. Ni, *Chemical Engineering & Technology* 32 (2009) 1484–1493.
- [35] Y. Lin, S.B. Beale, *Applied Mathematical Modelling* 30 (2006) 1485–1496.
- [36] R. Suwanwarangkul, E. Croiset, M.D. Pritzker, M.W. Fowler, P.L. Douglas, E. Entchev, *Journal of Power Sources* 154 (2006) 74–85.
- [37] C. Bao, Y. Shi, E. Croiset, C. Li, N. Cai, *Journal of Power Sources* 195 (2010) 4871–4892.
- [38] F. Calise, G. Ferruzzi, L. Vanoli, *Applied Energy* 86 (2009) 2401–2410.
- [39] R. Bove, S. Ubertini, *Journal of Power Sources* 159 (2006) 543–559.
- [40] C.O. Colpan, I. Dincer, F. Hamdullahpur, *International Journal of Energy Research* 32 (2008) 336–355.
- [41] A. Faghri, Z. Guo, *International Journal of Heat and Mass Transfer* 48 (2005) 3891–3920.
- [42] S. Kakac, A. Pramuanjaroenkij, X.Y. Zhou, *International Journal of Hydrogen Energy* 32 (2007) 761–786.
- [43] S. Cordiner, A. Mariani, V. Mulone, *Journal of Heat Transfer* 132 (2010) 062801.
- [44] J.R. Izzo, A.A. Peracchio, W.K.S. Chiu, *Journal of Fuel Cell Science and Technology* 7 (2010) 031017.
- [45] P.W. Li, K. Suzuki, *Journal of The Electrochemical Society* 151 (2004) A548–A557.
- [46] Y.X. Lu, L. Schaefer, P.W. Li, *Journal of Power Sources* 140 (2005) 331–339.

- [47] H. Mounir, A. El Gharad, M. Belaiche, M. Boukalouch, *Energy Conversion and Management* 50 (2009) 2685–2692.
- [48] K.J. Kattke, R.J. Braun, *Journal of Power Sources* 196 (2011) 6347–6355.
- [49] D. Cui, M. Cheng, *AIChE Journal* 55 (2009) 771–782.
- [50] R. Suwanwarangkul, E. Croiset, M.D. Pritzker, M.W. Fowler, P.L. Douglas, E. Entchev, *Journal of Power Sources* 166 (2007) 386–399.
- [51] D. Sanchez, R. Chacartegui, A. Munoz, T. Sanchez, *Journal of Power Sources* 160 (2006) 1074–1087.
- [52] J. Park, J. Bae, J.-Y. Kim, *Renewable Energy* 42 (2012) 180–185.
- [53] P.W. Li, M.K. Chyu, *Journal of Power Sources* 124 (2003) 487–498.
- [54] M. Andersson, J. Yuan, B. Sundén, *International Journal of Heat and Mass Transfer* 55 (2012) 773–788.
- [55] M.F. Serincan, U. Pasaogullari, N.M. Sammes, *Journal of The Electrochemical Society* 155 (2008) B1117–B1127.
- [56] Q. Wang, L. Li, C. Wang, *Journal of Power Sources* 186 (2009) 399–407.
- [57] N. Autissier, D. Larrain, J. Van Herle, D. Favrat, *Journal of Power Sources* 131 (2004) 313–319.
- [58] P. Sarkar, L. Yamarte, H.S. Rho, L. Johanson, *International Journal of Applied Ceramic Technology* 4 (2007) 103–108.
- [59] S. Amiri, R.E. Hayes, K. Nandakumar, P. Sarkar, *Chemical Engineering Science* 65 (2010) 6001–6013.
- [60] R.B. Bird, W.E. Stewart, E.N. Lightfoot, *Transport Phenomena*, second ed., J. Wiley, New York, 2002.
- [61] W.B. Gu, C.Y. Wang, *Journal of The Electrochemical Society* 147 (2000) 2910–2922.
- [62] D.L. Damm, A.G. Fedorov, *Journal of Power Sources* 159 (2006) 1153–1157.
- [63] K. Fischer, J.R. Seume, *Journal of Fuel Cell Science and Technology* 6 (2009) 011002.
- [64] S.K. Ratkje, Y. Tomii, *Journal of The Electrochemical Society* 140 (1993) 59–66.
- [65] A. Voigt, N. Hanssen, C. Weichmann, *Mathematical and Computer Modelling* 39 (2004) 145–150.
- [66] C. Weichmann, R. Backofen, A. Voigt, *Advanced Computational Methods in Heat Transfer VIII*, WIT Press, Lisbon, Portugal, 2004, pp. 313–322.
- [67] M.F. Cohen, D.P. Greenberg, *ACM Computer Graphics* 19 (1985) 31–40.
- [68] A.J. Rankin, R.E. Hayes, S.T. Kolaczowski, *Chemical Engineering Research & Design* 73 (1995) 110–121.
- [69] D. Sanchez, A. Munoz, T. Sanchez, *Journal of Power Sources* 169 (2007) 25–34.
- [70] B. Todd, J.B. Young, *Journal of Power Sources* 110 (2002) 186–200.
- [71] T.E. Daubert, R.P. Danner, *Design Institute for Physical Property Data (U.S.), Physical and Thermodynamic Properties of Pure Chemicals: Data Compilation*, Hemisphere Pub. Corp., New York, 1989.
- [72] J.R. Ferguson, J.M. Fiard, R. Herbin, *Journal of Power Sources* 58 (1996) 109–122.
- [73] Chemical Rubber Company, *Handbook of Chemistry and Physics*, CRC Press, Cleveland, 2004.
- [74] K.-H. Hellwege, J.L. Olsen, *Landolt-Börnstein – Group III Condensed Matter*, v. 15a, Springer, Berlin Heidelberg, 1983.
- [75] H.Y. Zhu, R.J. Kee, V.M. Janardhanan, O. Deutschmann, D.G. Goodwin, *Journal of The Electrochemical Society* 152 (2005) A2427–A2440.
- [76] J.F. Shackelford, W. Alexander, *CRC Materials Science and Engineering Handbook*, third ed., CRC Press, Boca Raton, FL, 2001.
- [77] L. Petrucci, S. Cocchi, F. Fineschi, *Journal of Power Sources* 118 (2003) 96–107.
- [78] Purdue University, *Thermophysical Properties Research Center, Y.S. Touloukian, Thermophysical Properties of Matter [The TPRC Data Series; a Comprehensive Compilation of Data]*, IFI/Plenum, New York, 1970.